Shear-induced collective diffusivity down a concentration gradient in a viscous emulsion of drops

Abhilash Reddy Malipeddi[1] **and Kausik Sarkar**[1,†]

[1]Department of Mechanical and Aerospace Engineering, The George Washington University, Washington, DC 20052, USA

The shear-induced collective diffusivity down a concentration gradient in a viscous emulsion is computed using direct numerical simulation. A layer of randomly packed drops subjected to a shear flow, shows the layer width to increase with the 1/3 power of time, consistent with a semi-dilute theory that assumes a diffusivity linear with concentration. This characteristic scaling and the underlying theory are used to compute the collective diffusivity coefficient. This is the first ever computation of this quantity for a system of deformable particles using fully resolved numerical simulation. The results match very well with previous experimental observations. The coefficient of collective diffusivity varies non-monotonically with the capillary number, due to the competing effects of increasing deformation and drop orientation. A phenomenological correlation for the collective diffusivity coefficient as a function of capillary number is presented. We also apply an alternative approach to compute collective diffusivity, developed originally for a statistically homogeneous rigid sphere suspension – computing the dynamic structure factor from the simulated droplet positions and examining its time variation at small wavenumber. We show that the results from this alternative approach qualitatively agree with our computation of collective diffusivity including the prediction of the non-monotonic variation of diffusivity with the capillary number.

Key words: drops, emulsions, multiphase flow

---

1. Introduction

Suspended non-Brownian particles in a sheared emulsion or suspension experience shear-induced diffusion due to irreversible inter-particle hydrodynamic and other interactions (Eckstein, Bailey & Shapiro 1977; Davis 1996). Shear-induced diffusion plays a critical role in chemical process engineering and microfluidic technologies by enhancing mixing (Lopez & Graham 2008) in low Reynolds number flows which is otherwise limited by slow molecular diffusion. In blood vessels, the radial concentration profile of blood cells is a result of the competition between shear-induced diffusion and wall-induced migration of cells towards the centre

† Email address for correspondence: sarkar@gwu.edu

(Grandchamp *et al.* 2013). The mechanical properties of a blood cell, such as stiffness that influences shear-induced diffusivity, are a proxy for the health of the cells (Cooke, Mohandas & Coppel 2001). More fundamentally, the spatial distribution of particles caused by the diffusion determines the local and global rheology of the flow. Here, we propose a direct numerical simulation technique and compute for the first time the collective diffusivity in a non-dilute emulsion of viscous drops.

In suspensions of rigid spheres, under the assumption of Stokes flow, hydrodynamic pair interaction is reversible. A symmetry breaking mechanism such as roughness is needed to give rise to diffusion from two-particle interactions (da Cunha & Hinch 1996). In case of drops or other deformable particles, pairwise hydrodynamic interaction is irreversible and nonlinear (Olapade, Singh & Sarkar 2009; Singh & Sarkar 2009; Sarkar & Singh 2013) leading to a diffusive behaviour (Loewenberg & Hinch 1997). Shear-induced diffusion is generally separated into self-diffusion and collective or gradient diffusion (Rallison & Hinch 1986; Rusconi & Stone 2008). The first refers to the random walk-like motion exhibited by the particles and is present even in a uniformly mixed suspension or emulsion. It is characterized by the self-diffusion coefficient $D_s = \dot{\gamma} a^2 f_s(\phi)$ with $\dot{\gamma}$ being the shear rate, a the particle radius and $f_s(\phi)$ the non-dimensional self-diffusivity, a function of the particle volume fraction ϕ. The collective diffusion refers to a diffusive flux $-D_c \nabla \phi$ in the presence of a particle concentration gradient and is similar to Fickian diffusion (Leshansky, Morris & Brady 2008). The non-dimensional collective diffusivity $f_c(\phi) = D_c/\dot{\gamma} a^2$ is usually higher in magnitude than $f_s(\phi)$. Both diffusion coefficients depend on the flow and are generally anisotropic.

Investigation into flow-induced diffusion was initiated by Eckstein *et al.* (1977). They experimentally measured the lateral displacement of a tagged particle in a Couette flow to compute the self-diffusivity. Subsequently, numerous experimental, theoretical and computational studies explored various aspects of shear-induced diffusion. The collective diffusivity was for the first time indirectly inferred in the vorticity direction from the transient viscosity changes that were observed in a Couette flow viscometer (Leighton & Acrivos 1987). The changes were caused by the diffusion of particles from the high shear region (Couette gap) to the low shear region (fluid reservoir). A more robust procedure for computing self-diffusivity was developed using the time taken for a visually detectable particle to go around the Couette cell in successive revolutions (Leighton & Acrivos 1987). Instead of tracking a single particle that requires long temporal data to ensure ergodicity, positions of multiple tracer particles were recorded using a digital camera, reducing the time requirement by an order of magnitude and enabling the capture of the transient features of self-diffusion (Breedveld *et al.* 1998; Breedveld 2000). More recent experiments (Rusconi & Stone 2008) have used microfluidic devices to measure the collective diffusivity in the vorticity direction of highly asymmetric plate-like particles. On the numerical side, pairwise interactions between two particles with surface roughness have been used to calculate the self- and collective diffusivities in the dilute regime (da Cunha & Hinch 1996). The diffusion was assumed to be exclusively due to two-particle interactions, and the diffusivities were calculated by integrating the displacement over all possible initial positions of the two particles. Stokesian dynamics (Brady & Bossis 1988) has been used to calculate the self-diffusivity for colloidal (Foss & Brady 1999) and non-colloidal (Sierou & Brady 2004) suspensions directly from an ensemble averaged mean square displacement of the particles, and also by using the velocity autocorrelation function. The collective diffusivity was calculated from simulations of homogeneous suspensions (Marchioro & Acrivos 2001), using the fact that the

rate of relaxation of the microstructure on perturbation is proportional to the gradient diffusivity. A more robust method for calculating the all particle diffusivities from a single statistically homogeneous simulation using the dynamic structure factor of a sheared suspension has also been developed (Morris & Brady 1996; Leshansky & Brady 2005; Leshansky *et al.* 2008).

In contrast to suspensions, there have been far fewer studies devoted to shear-induced diffusivity in emulsions. King & Leighton (2001) did the first measurement of collective diffusivity, but the values they reported were lower than theoretical predictions, due to the presence of surfactants that were required to stabilize the droplets against coalescence. Hudson (2003), using more viscous liquids that did not require surfactants, was the first to accurately measure the collective diffusivities of an emulsion. To our knowledge, there have been no experimental measurements of self-diffusivity in emulsions of drops. Self-diffusivities of red blood cells (Higgins *et al.* 2009), and red blood cell ghosts (Goldsmith & Marlow 1979; Cha & Beissinger 2001) have been measured experimentally. Grandchamp *et al.* (2013) reported an experimental study of the collective diffusivity of red blood cells in a rectangular channel (also see Podgorski *et al.* 2011; Bureau *et al.* 2017). While we could not find any computation of the collective diffusivity in emulsions, computations of self-diffusivity have been attempted by computing two drop trajectories in shear and averaged mean square displacements by Loewenberg & Hinch (1997) using a boundary integral simulation of the Stokes flow. Tan, Le & Chiam (2012) simulated emulsions of capsules in a bounded shear flow to estimate the self-diffusivity in the vorticity direction. They showed that the emulsion can be sub-diffusive, diffusive or super-diffusive depending on the level of confinement. Pairwise simulations of vesicles have been used to calculate their self-diffusivity (Zhao & Shaqfeh 2013; Gires *et al.* 2014). Calculating collective diffusivity with this method has not been possible for deformable particles, as the integral over all possible pair of drops is convergent only for zero capillary number, i.e. undeformed drops (King & Leighton 2001; Gires *et al.* 2014). In the past, renormalization procedures have been applied to such divergent integrals; they use global constraints to obtain convergent expressions for effective stresses and sedimentation velocity (Batchelor 1972; Batchelor & Green 1972) as well as shear-induced diffusion coefficients in a suspension (Wang, Mauri & Acrivos 1998). Such procedures have not been applied to the current problem.

We use a direct numerical simulation of a layer of randomly packed drops in a shear flow to compute the collective diffusivity varying the capillary number. In the following, we briefly describe the numerical method and our procedure to obtain the collective diffusivity from the simulation of a relatively small number of particles over a short time interval. We also provide a qualitative analysis of the shear induced diffusivity using the dynamic structure factor approach (Leshansky & Brady 2005) that is based on the theory of dynamic light scattering. We discuss computed results, compare with previous experimental observations and offer a brief conclusion.

2. Simulation method

We solve the incompressible Navier–Stokes equations using a front-tracking method (Tryggvason *et al.* 2001):

$$\nabla \cdot \boldsymbol{u} = 0,$$

$$\frac{\partial(\rho\boldsymbol{u})}{\partial t} + \nabla \cdot (\rho\boldsymbol{u}\boldsymbol{u}) = -\nabla p + \nabla \cdot [\mu\{\nabla\boldsymbol{u} + (\nabla\boldsymbol{u})^{\mathrm{T}}\}] - \int_{\partial B} \kappa\boldsymbol{n}\sigma\delta(\boldsymbol{x} - \boldsymbol{x}')\,\mathrm{d}S(\boldsymbol{x}').$$

$$(2.1)$$
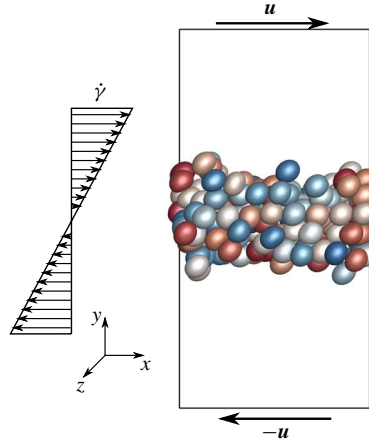
FIGURE 1. (Colour online) A sketch of the problem being simulated.

Here $\boldsymbol{u}$, p, ρ and μ are the velocity, pressure, density and viscosity respectively. κ is the local drop surface curvature, $\boldsymbol{n}$ is the unit outward normal to the surface ∂B of all drops and σ is the interfacial tension. In this numerical method, all drops and their interactions are resolved. The method has been used by our group in many problems involving drops (Sarkar & Schowalter 2001) and capsules (Li & Sarkar 2008) in viscous and viscoelastic fluids (Sarkar & Schowalter 2000; Mukherjee & Sarkar 2009, 2013), including pairwise interactions (Singh & Sarkar 2009, 2015; Sarkar & Singh 2013) and dense emulsions (Srivastava, Malipeddi & Sarkar 2016). The reader is referred to these earlier publications for the details of the algorithm and its verification and validation.

    To compute the diffusion in a shear flow, we numerically simulate drops initially concentrated in a central layer subjected to a simple unbounded shear flow (figure 1). This is a departure from the experiments of King & Leighton (2001) or Hudson (2003), where drops were initially uniformly distributed between the walls and experience a bounded shear. The wall-induced lateral migration of drops away from the walls (Mukherjee & Sarkar 2013, 2014; Sarkar & Singh 2013; Singh, Li & Sarkar 2013) competes with shear-induced collective diffusion to result in a concentration gradient towards the centre. In contrast, here the drops are not affected by walls. A uniform shear flow is generated in a computational domain, which is periodic in the x and z directions and has numerical walls in the y direction moving with specified velocities. The distance between the walls is $L_y = 28a$ (a is the drop radius), sufficiently large to simulate an unbounded shear (demonstrated below). The length of the domain in the x and z directions is $L_x = L_z = 14a$. A $96 \times 192 \times 96$ uniform grid is used in the computational domain leading to 15 grid points per drop diameter, shown to be sufficient in our earlier studies. The drops are initially randomly close packed (Desmond & Weeks 2009) in a thin ($\sim 0.2 L_y$) layer parallel to the xz-plane (figure 1) in the middle of the computational domain. In the x and z directions, the distribution of drops is homogeneous initially and remains so. The drops remain adequately separated from the y-boundaries such that the wall effects are negligible on drops over the time scale necessary to characterize the diffusion (discussed further below). The front tracking finite difference code is used to solve the fluid dynamics equation for various capillary numbers, the ratio between the viscous and interfacial
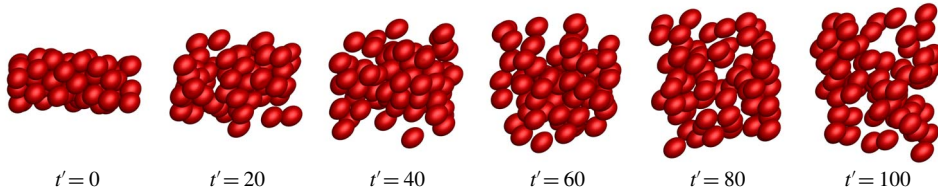
FIGURE 2. (Colour online) Snapshots from a simulation of 70 drops at $Ca = 0.10$ showing a layer of drops spreading due to collective diffusion in shear.

stresses $Ca = \mu \dot{\gamma} a / \sigma$. The drops are viscosity matched. Note that the explicit nature of the code prevents us from simulating Stokes flow. The simulations are performed at small but finite Reynolds number of $Re = \rho \dot{\gamma} a^2 / \mu = 0.1$. Previously we have shown that results at this Re matches sufficiently well with Stokes flow simulation of emulsions (Srivastava *et al.* 2016).

3. Collective/gradient diffusivity

Under the assumption of homogeneity in the x and z directions, the problem reduces to an unsteady, one-dimensional diffusion problem for the particle volume fraction $\phi = \phi(y, t)$:

$$\frac{\partial \phi}{\partial t} = \frac{\partial}{\partial y} \left(D_c \frac{\partial \phi}{\partial y} \right). \tag{3.1}$$

Assuming that two-particle interaction dominates the dynamics, the collective diffusivity is proportional to the rate of two-particle interactions (collisions) $\dot{\gamma} \phi$: $D_c = \dot{\gamma} \phi a^2 f_2$, (i.e. $f_{c,2} = f_2 \phi$) (da Cunha & Hinch 1996; Loewenberg & Hinch 1997; Rusconi & Stone 2008; Grandchamp *et al.* 2013). Here f_2 is the non-dimensional collective diffusivity in the velocity-gradient direction, the focus of the present work. The assumption of linear dependence of D_c on volume fraction, or equivalently the dominance of pairwise interaction is *a posteriori* justified by the simulation results.

The simulation shows that the drops spread in the gradient direction with time (figure 2; also see the movie in the supplemental material available online at https://doi.org/10.1017/jfm.2019.122). We non-dimensionalize time and length as $t = t'/\dot{\gamma}$, $y = y'a$. It has been shown by a detailed analysis that when a fixed number of particles spread due to shear-induced diffusion, the transformed equation (3.1) admits a self-similar parabolic concentration (Grandchamp *et al.* 2013)

$$\psi(\eta) = (f_2 t')^{1/3} \phi = \left(b - \eta^2 / 6 \right), \quad \eta = \frac{y'}{(f_2 t')^{1/3}}, \tag{3.2}$$

in the similarity variable η, where b is a free parameter. We see that the profile spreads with $t^{1/3}$, which is slower than $t^{1/2}$ growth known to occur in systems with a constant diffusivity (i.e. independent of concentration or volume fraction). Note that the characteristic scaling exponent depends on the details of the problem formulation. In case of particles spreading from one side in an initially Heaviside concentration profile (Rusconi & Stone 2008), the characteristic exponent is 1/2, even when $D_c = \dot{\gamma} \phi^m a^2 f_2$ with $m > 1$. In the experimental study of red blood cells (RBC) diffusing down a gradient (Grandchamp *et al.* 2013), authors observed the RBC concentration

to reach a self-similar parabolic concentration as predicted by the analytical solution (3.2) with its half-width at half-height, w, changing with time as

$$\underline{w}^3 - \underline{w}_o^3 = Kt', \quad K = \frac{9f_2 N_o}{(4\sqrt{2})}, \quad N_o = \int \phi(y', t') \, dy'. \tag{3.3}$$

Here $\underline{w}_o$ is the initial width and N_o is a conserved quantity, related to the particular nature of the problem mentioned before – a fixed number of particles diffusing out. It was used to obtain the value of the collective diffusivity f_2.

We use two different methods to determine collective diffusivity f_2 from our simulation. The first one follows closely the approach mentioned above – determine width by fitting a parabolic profile to the concentration and use the width-versus-time data as per (3.3). For the simulation, $N_o = NV/aL_x L_z$, where V is the drop volume and N is the total number of drops in the domain. However, to obtain a robust parabolic approximation of the concentration for width estimation, one needs densely sampled data with a very large number of drops as, in fact, were obtained in past experiments (King & Leighton 2001; Hudson 2003; Grandchamp *et al.* 2013). Obtaining similar quality data from a direct numerical solution of the Navier–Stokes equation requires expensive simulation with a large number of individually resolved drops in a large computational domain and a long simulation time. Figure 2 shows the time evolution of the drop layer over time from a typical simulation of 70 drops. As the layer of drops gets sparser, the quality of the concentration profile could become increasingly worse due to there not being enough drops in each bin, leading to problems with curve fitting. Instead of using drop centre positions to compute the profile, which would have restricted the resolution strictly to the drop size, we compute drop phase concentration over a far finer resolution ($1/30 \, a$).

We also use a second method for calculating f_2 – instead of the half-width w of the concentration profile, we use the standard deviation w of the y-positions (y'_i) of N drops (figure 2) as a representative of the width:

$$w = \sqrt{\frac{1}{N} \sum_{i=1}^{N} (y'_i - \mu)^2}, \quad \mu = \frac{1}{N} \sum_{i=1}^{N} y'_i. \tag{3.4}$$

Theory predicts this 'modified' width relative to its initial value w_0 to also increase linearly with time with a slightly different constant than in (3.3)

$$w^3 - w_o^3 = K't', \quad K' = \frac{9f_2 N_o}{(10\sqrt{5})}. \tag{3.5}$$

From the drop locations in a typical simulation (e.g. figure 2), w is calculated and plotted on a log–log plot to show an eventual linear curve indicating the power-law dependence on time and f_2 is computed. This way of computing f_2 avoids curve fitting at every time step and the associated errors. However, we will see that both methods lead to very similar values of f_2.

4. Results and discussion

4.1. *Collective diffusivity using two methods at $Ca = 0.05$*

Figure 2 shows a typical case of an initially concentrated layer of viscous drops experiencing shear-induced diffusion with time. Figure 3(*a*) plots individual drop
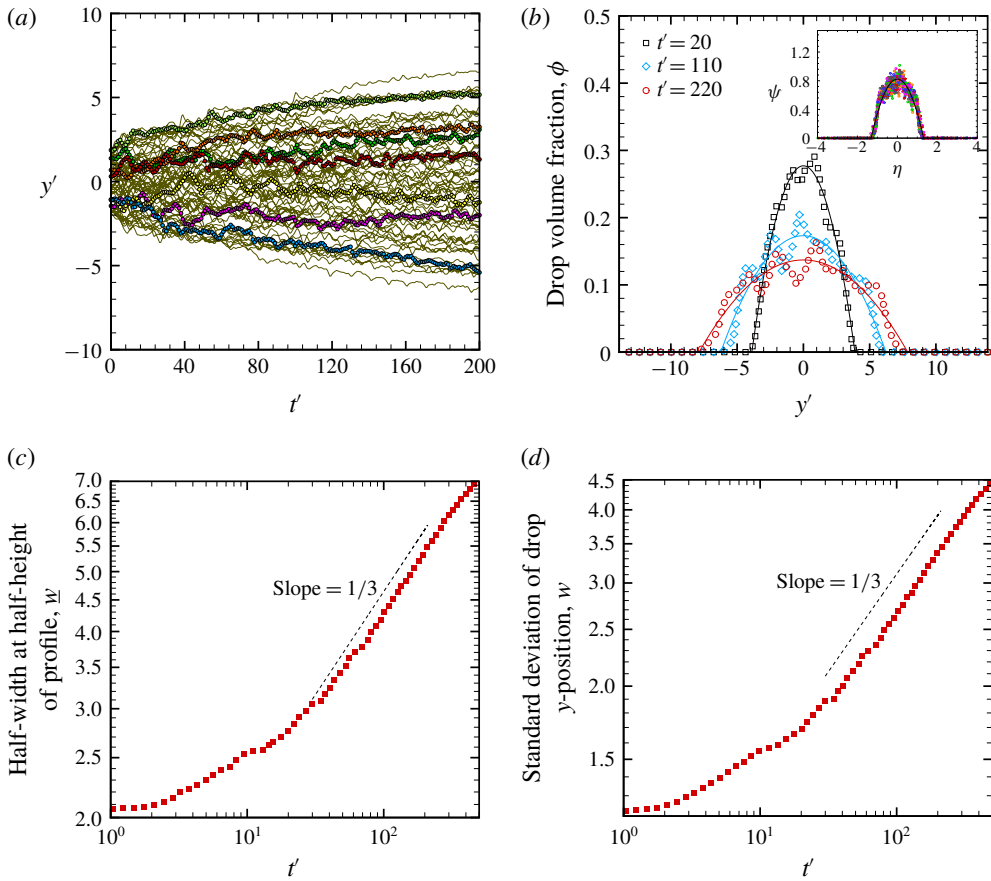
FIGURE 3. (Colour online) (*a*) The drop positions versus time at $Ca = 0.05$. A few drop tracks are coloured to highlight the random-walk-like movement. (*b*) Concentration profile at various times of drops spreading in shear at $Ca = 0.05$. Solid lines are the best fit parabola. The inset shows the same scaled with $t^{1/3}$ (as per (4.1)) collapse of different time curves due to the self-similar evolution. (*c*) Width at half-height of the concentration profile as a function of time on a log–log plot, showing the $1/3$ exponent scaling. (*d*) Modified width based on the standard deviation of the drop position as a function of time showing the same scaling.

positions with time for a low capillary number of $Ca = 0.05$. The drops exhibit a random-walk-like movement. The concentration profile for this case is plotted in figure 3(*b*), fitting a parabolic profile in successive time instants (also see the movie in the supplemental material). In the inset of figure 3(*b*), we plot the concentration profiles scaled by $t'^{-1/3}$ versus $y'/t'^{1/3}$ to see that indeed they all collapse as they should according to the similarity profile $\psi(\eta)$ described in (3.2). Plotting the width $\underline{w}$ on a log–log plot in figure 3(*c*) shows an eventual linear curve indicating the $1/3$ power-law dependence on time. The initial data ($t' < 20$) are discarded; starting from $t_0' = 20$, the remaining portion is subdivided into smaller time intervals (15 inverse shear units). The slope of $\underline{w}^3 - \underline{w}_o^3$ in each subinterval and the corresponding value of f_2 there according to (3.3) is computed. The dynamics over these different time intervals are approximately uncorrelated (Zinchenko & Davis 2002). The mean of this average is reported (under the assumption of ergodicity, it is equal to an ensemble
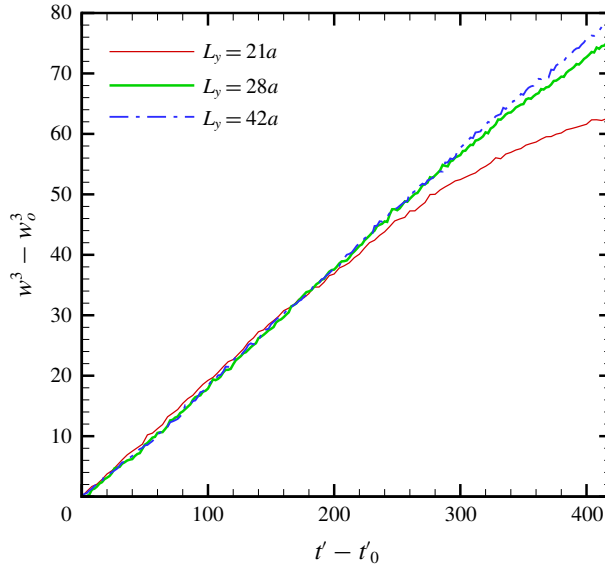
FIGURE 4. (Colour online) Effect of the computational domain: the width of drop layer as a function of time for different widths of the computational domain.

average). The corresponding standard deviation of the values from different time intervals is reported as the uncertainty of the estimation. We obtain $f_2 = 0.329 \pm 0.02$. In figure 3(d), the plot of the standard deviation w of the layer according to (3.4) against time also shows a similar 1/3 slope with time. An identical analysis is executed on this data to obtain the average f_2 according to the second method to obtain $f_2 = 0.327 \pm 0.021$, very similar to the one obtained by the other method. Note that there is minimal 'noise' in both curves in figure 3(c,d), demonstrating the robust nature of the 1/3 exponent. Presence of noise detracts from the confidence of the fitting; which is why ensemble averaging of mean square displacements in the computation of self-diffusivity requires a significantly larger number of particles (Marchioro & Acrivos 2001).

4.2. *Effects of domain size*

Although we are interested in computing the collective diffusivity in an emulsion in a free shear flow, i.e. without any boundary, our code requires walls to generate the shear flow. Therefore, it is important to show that the domain size chosen is sufficiently large and that the results are independent of the physical dimensions of the domain. The pairwise interaction between drops in a shear flow with walls was shown to be exactly the same as the free-shear interaction for $L_y \geqslant 25a$ when the drops are at the centre of the domain (Singh & Sarkar 2015). However, unlike that case, the layer of drops considered here spreads its thickness with time and eventually would be affected by the walls. Figure 4 shows $w^3 - w_o^3$ increasing with time for three different separations L_y between the walls. All three curves are linear for a substantial portion initially and all have the same slope. This shows that, in this linear region the walls do not affect the dynamics of the drops. For $L_y = 21a$, at approximately $t' - t'_0 = 200$, the linearity breaks down due to the wall effects. For $L_y = 28a$, this happens at approximately $t' - t'_0 = 300$ and for $L_y = 42a$ there is no

L_y/a	f_2
21	0.328 ± 0.022
28	0.327 ± 0.021
42	0.329 ± 0.024

TABLE 1. Effect of domain length in the y direction, i.e. the distance between the walls, on the diffusivity.

L_x/a	f_2
10	0.313 ± 0.030
12	0.314 ± 0.036
14	0.327 ± 0.021
28	0.336 ± 0.032

TABLE 2. Effect of domain length in the flow direction on the diffusivity.

noticeable deviation in the curve until approximately $t' - t'_0 = 400$. Table 1 shows the values of the diffusivity calculated in each of these cases from the linear portion. We obtain a similar value for all three cases with no particular trend. We choose $L_y = 28a$ for all subsequent simulations. For this wall separation, one can estimate the lateral velocity on a droplet induced by the bounding walls using a small deformation analysis (Chan & Leal 1979):

$$\frac{V_{lat}}{\dot{\gamma} a} = -\frac{3(16 + 19\lambda)(54\lambda^2 + 97\lambda + 54)}{4480(1 + \lambda)^3} Ca \left(\frac{a}{L_y}\right)^2 \left(\frac{y}{L_y}\right) \left(1 + \frac{8}{(1 - 4y^2/L_y^2)^2}\right). \quad (4.1)$$

For a sample case of $Ca = 0.1$, the half-width of the spreading layer reaches $y \sim 4.5a$. With a local volume fraction of ~ 0.1, one obtains a Péclet number of $Pe = V_{lat}/(f_2 \dot{\gamma} a \phi) \sim 0.02$, indicating negligible effects of the walls. We also study the effects of L_x, shown in table 2. In the interest of a reasonable computation time, $L_x = 14a$ is chosen which seems sufficient for our purpose.

4.3. *Effects of N_o (initial volume fraction in the layer) and initial configuration*

In addition to the $t^{1/3}$ scaling of the width, the dependence of diffusivity on the quantity N_o that appears in (3.3) and (3.5) shows that the diffusion is mediated by inter-particle interactions. In experiments at high volume fractions (>0.3), the effective coefficient of diffusion (K in (3.3)) increased quadratically with N_o, indicating a non-negligible contribution from three-particle interactions (Grandchamp *et al.* 2013). It results in a linear increase of f_2 with N_o. If only pairwise interactions dominate, f_2 is expected to be independent of N_o. To verify this and to ensure that the size of the system is sufficient, we perform simulations with different initial configurations and different N_o. Different N_o values represent different volume fractions in the central layer at $t' = t'_0$ (after the power law sets in as seen in figure 3c,d) – e.g. the curves for $N_o = 1.44$ and 3.28 correspond to 18 % and 31 % volume fraction. The curve for $N_o = 2.44$ with an asterisk is for a volume fraction of 49 % obtained with an initial configuration with a smaller initial layer width. They also represent different layer widths from ~ 6 to ~ 8 drop radii as well as different initial random configurations.
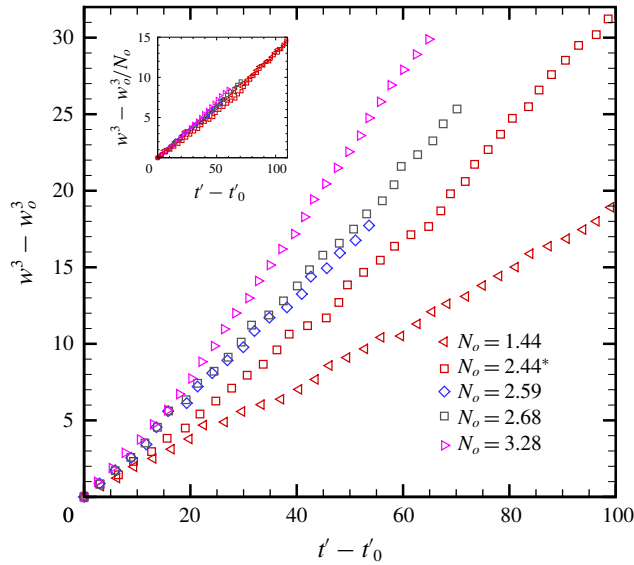
FIGURE 5. (Colour online) Width of the drop layer as a function of time for $Ca = 0.05$ in the power law regime for different values of N_o. Inset shows the same, scaled by N_o, collapses onto a single curve.

Figure 5 shows $w^3 - w_o^3$ versus time for these various cases. As expected from (3.5) the slope increases with N_o. The inset shows that upon scaling with N_o all lines collapse onto a single line, indicating that the results are independent of N_o as well as initial configurations.

Note that the relation $w^3 \propto t$ arising from (3.2) is contingent on the assumption of the dominance of pair interactions in determining the shear-induced diffusion, that gave rise to $D_c \propto \phi$. In contrast, if three-particle interactions were to dominate, the diffusivity would be proportional to ϕ^2 giving rise to $w^4 \propto t$ (Grandchamp *et al.* 2013). In general, at high enough concentrations, one would expect the higher-order interactions to be significant, and a clear scaling might not appear. In the initial part of the data in figure 3(*c*,*d*), when the local volume fraction is high in the closely packed layer, the deviation from the 1/3 scaling – slopes are smaller – could be a signature of higher-order interactions in addition to the deviation from the parabolic profile. With time the local volume fraction continues to decrease and eventually higher than two-drop interactions become increasingly rare. Note that the time scale of drop deformation, the capillary time scale, is quite small – identical to Ca in shear unit, i.e. 0.05–0.35 for the cases considered here. Therefore, the drops achieve their final deformed state long before the 1/3 scaling behaviour sets in. Based on the scaling seen in figure 5 and the corresponding volume fractions (specifically the curve for $N_o = 2.44$), we conclude that the 1/3 scaling (and the relationship $D_c \propto \phi$) holds for $\phi \leqslant \sim 0.5$.

4.4. *Effects of capillary number*

Figure 6 shows the drops at three different capillary numbers at approximately the same time when the drops achieve their deformed shapes. We compute the non-dimensional collective diffusivity f_2 using both methods at different capillary
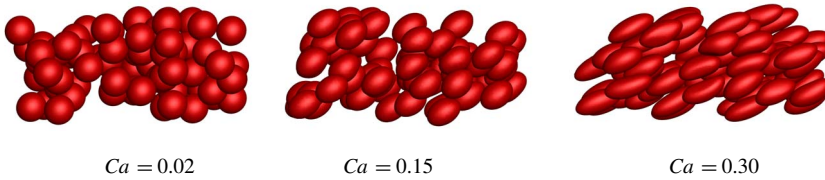
$$Ca = 0.02 \qquad Ca = 0.15 \qquad Ca = 0.30$$

FIGURE 6. (Colour online) Snapshots of the drop layer at $t' = \sim 17$ for three different Ca.
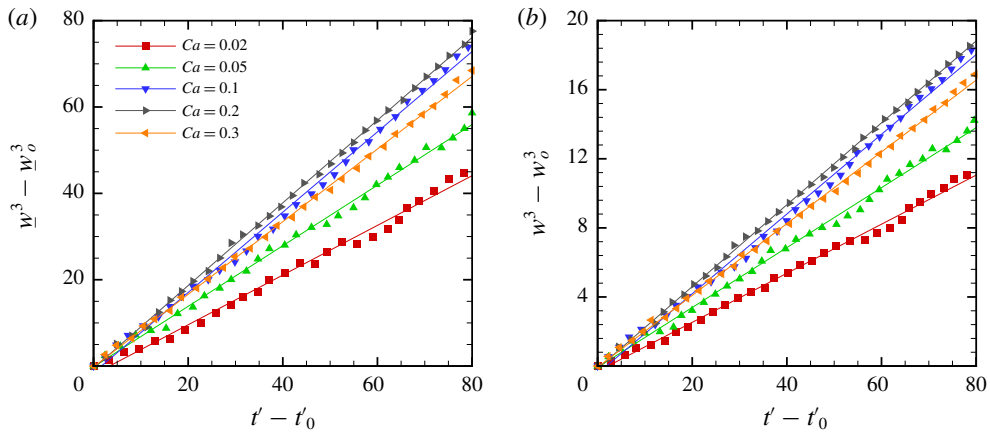

FIGURE 7. (Colour online) (*a*) Width at half-height of the concentration profile as a function of time for different Ca. (*b*) Modified width of the drop layer as a function of time for different Ca. Cube of both quantities has been plotted to show their linear scaling.

numbers. Figure 7(*a*,*b*) shows that $\underline{w}^3 - \underline{w}_o^3$ and $w^3 - w_o^3$ both vary linearly and almost identically with $t' - t'_0$ at different Ca values. Therefore, f_2 (the slopes) computed by the two methods are very similar at all values of Ca, as has been tabulated in table 3. In figure 8, we plot f_2 versus Ca using both methods. They resulted in very similar values. It shows a non-monotonic variation, as was also seen for the self-diffusivity (Loewenberg & Hinch 1997; Tan *et al.* 2012). An intuitive explanation for the non-monotonic variation can be obtained as arising from a competition between the effects of increasing deformation and decreasing drop orientation angle with increasing Ca in pair interactions. The time variation of the average deformation and average inclination angle of the drops are plotted in figure 9. As noted before, the initially spherical drops quickly reach their equilibrium deformation over the capillary time scale $t'_{capillary} = Ca$. The inclination angle starts at the inclination of the extensional axis $45°$ and decreases due to deformation (Taylor 1934). The fluctuations in their values are caused by the drop–drop interactions in the shear flow. Note that although the local volume fraction decreases due to diffusion of the drops, the average values of deformation and inclination angle do not change significantly over the time period considered.

In figure 9, we plot the Taylor deformation parameter $D = (L - B)/(L + B)$ (L and B are the maximal and the minimal distances of the drop surface from the centroid) averaged over all drops and over the power-law regime shown in figure 3(*c*,*d*); it approximately matches with the small deformation perturbative result $D = Ca(19\lambda +$
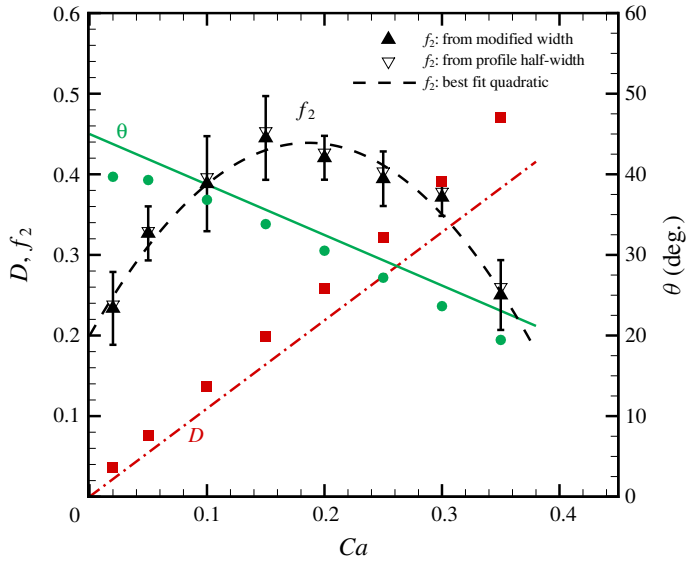
FIGURE 8. (Colour online) Dimensionless gradient diffusivity (f_2), deformation parameter (D) and drop inclination angle (θ) plotted as functions of Ca. Symbols are the results from the simulation. The solid and dash-dotted lines are predictions of small deformation perturbative analysis for θ and D respectively. The dashed line is a quadratic fit of the simulated f_2 values (solid triangles) obtained by standard deviation according to (4.2). The error bar corresponds to the f_2 values.
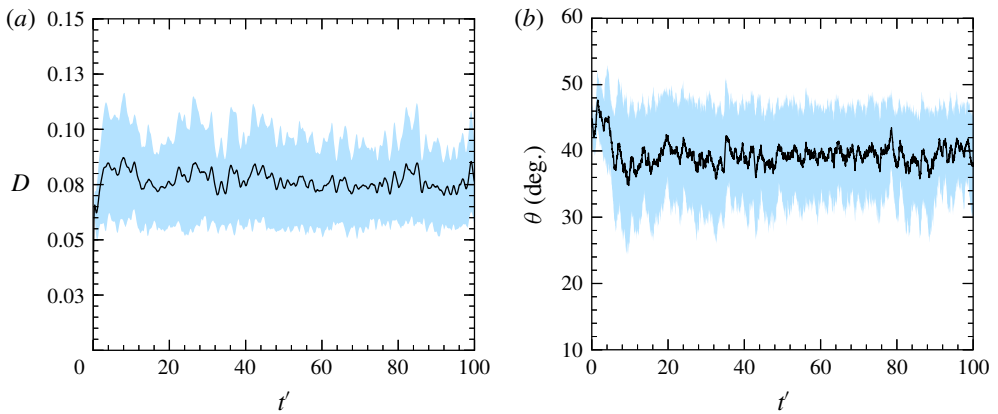

FIGURE 9. (Colour online) Average deformation (*a*) and average orientation angle (*b*) with time for a simulation at $Ca = 0.05$. The shading shows the standard deviation.

$16)/(16\lambda + 16)$ (λ is the viscosity ratio) (Taylor 1934) for the entire range of the Ca considered here, the deviation also resulting from the interactions. The average drop inclination angle plotted in the same figure (figure 9) shows a decrease as also predicted by the small deformation perturbative analysis $\theta = \pi/4 - Ca(2\lambda + 3)(19\lambda + 16)/(80\lambda + 80)$ (Chaffey & Brenner 1967).

Figure 10 explains the effects of competition between increasing deformation and decreasing inclination with increasing Ca. For small Ca, increased deformation with
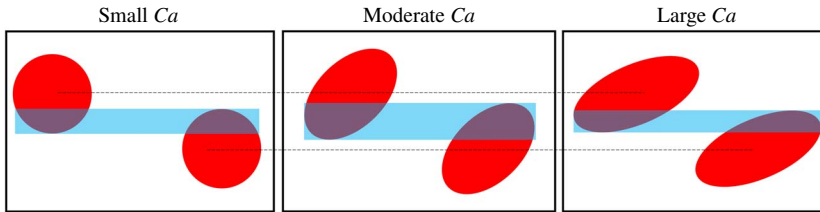
FIGURE 10. (Colour online) Schematic showing two approaching drops in three different regimes of *Ca* to explain the non-monotonic dependence of f_2 on *Ca*. The overlapping region increases initially and then decreases.

Ca	f_2 from *w*	f_2 from $\underline{w}$
0.02	0.23 ± 0.05	0.24 ± 0.06
0.05	0.33 ± 0.03	0.33 ± 0.03
0.10	0.39 ± 0.06	0.40 ± 0.06
0.15	0.45 ± 0.05	0.45 ± 0.05
0.2	0.42 ± 0.03	0.43 ± 0.03
0.25	0.39 ± 0.03	0.40 ± 0.03
0.30	0.37 ± 0.02	0.38 ± 0.03
0.35	0.25 ± 0.04	0.26 ± 0.05

TABLE 3. Tabulated values of f_2 using two methods, (i) from standard deviation of the droplet position and (ii) width of the concentration profile.

increasing *Ca* enhances the irreversible relative displacement between droplets upon interactions increasing the diffusivity. However, with larger increase in *Ca*, as the angle of inclination decreases, the drops are more aligned, allowing sliding, and eventually this effect overcomes the other, decreasing the diffusivity above $Ca \sim 0.2$. The non-monotonic variation in relative displacement in the pair collisions between drops in shear has been investigated in detail in the past (Olapade *et al.* 2009). Loewenberg & Hinch (1997) also found non-monotonicity in self-diffusivity versus *Ca*, and attributed it to the subtle difference in pairwise interactions between initially closely spaced drops at low and high *Ca* numbers. At low *Ca*, initially closely spaced drops experience higher post-collision net displacements in their streamlines compared to drops which are initially far apart; the converse is true at higher *Ca*. The authors argued that the balance between the decreasing near-field influence and the increasing far-field influence may have caused the non-monotonicity. Finally, we fitted the simulated values of f_2 for different *Ca* by a quadratic curve and obtained a phenomenological relation

$$f_2 = -6.89 Ca^2 + 2.57 Ca + 0.20. \qquad (4.2)$$

The relation has been plotted in figure 8.

4.5. *Comparison with past experiments and theory*

The only experimental measurement of f_2 available in the literature is the one reported by Hudson (2003), who used drops of poly(propylene glycol) or poly(ethylene-alt-propylene) dispersed in poly(ethylene glycol). We ran simulations with material

	Experimental f_2 (Hudson 2003)	Present work
$Ca = 0.02$	0.21	0.23
$Ca = 0.05$	0.16	0.27
$Ca = 0.40$	0.22, 0.25	—

TABLE 4. Comparison of the diffusivity calculated from the present simulations compared to the experimental values reported by Hudson (2003).

properties and a capillary number corresponding to this experiment and computed the diffusivity. The comparison with the experiment, shown in table 4, is very good at $Ca = 0.23$ but shows some departure at $Ca = 0.05$. At the large value of $Ca = 0.40$, the simulation indicated drop break-up. In search of possible reasons for the difference between the computed results and measurements, one notes that the current simulation is for a purely monodisperse system and without any coalescence. However, Hudson noted that in their experiment the coalescence is rare and polydispersity is minor (the ratio between volume averaged and number averaged radii is ∼1.2).

In the limit of $Ca \to 0$, the collective diffusivity for an emulsion of spherical drops was inferred from two drop interactions to be ∼0.20 (Ramachandran, Loewenberg & Leighton 2010), which matches with the value obtained by extrapolating the present numerical result. There have been no other computations of f_2 in the literature. Grandchamp *et al.* (2013) reported a value of ∼0.77 (rescaled by particle volume) for red blood cells. Loewenberg & Hinch (1997) used boundary element simulation of pair collisions to obtain self-diffusivity 8–9 times smaller than the gradient diffusivity calculated here. As noted before, for emulsions, effort to compute the gradient diffusivity by integrating all possible pair collisions has been frustrated due to divergence of the integrals. However, for rough spheres pair collisions can be used to predict both diffusivities and the ratio of gradient to self-diffusivity has been found to be ∼6 (da Cunha & Hinch 1996), similar to what has been found here.

4.6. *Collective diffusivity computed using dynamic structure factor*

As noted in the Introduction, Leshansky & Brady (2005) provided an elegant means of computing the collective diffusivity of a rigid sphere suspension from the simulation of a statistically homogeneous suspension in simple shear. It is based on the fact that even in a homogeneous system, stochastic fluctuations appear spontaneously and their decay can be used to compute self- as well as collective diffusivities (Morris & Brady 1996). However, collective diffusivity intrinsically is a property of a non-homogeneous system with concentration gradients. Therefore, it will be of interest to apply any methodology for computing collective diffusivity to a non-homogeneous system. Here, we apply the method proposed by the above authors to our system, get an estimate of the collective diffusivity, qualitatively compare with the values obtained in the previous section and discuss the applicability of the results.

The dynamic structure factor approach to obtaining the collective diffusivity stemmed from the theory of dynamic light scattering, where the scattered response of a monochromatic beam of a laser from a scattering volume containing multiple scatterers (large macromolecules such as DNA, proteins, amino acids, viruses and bacteria) is measured. The scattered field fluctuates due to thermal fluctuations of the molecules and can provide structural and dynamic information about the system (Berne & Pecora 1976). For an infinitely dilute system of non-interacting scatterers,

the autocorrelation of the fluctuation decays exponentially and the decay time is inversely proportional to the diffusivity. For concentrated systems, the fluctuating particle motions are however affected by their hydrodynamic interactions and the experimental observations require careful analysis (Altenberger & Deutch 1973; Altenberger 1979; Russel & Glendinning 1981) and proper interpretation, which then could furnish the collective or self-diffusivity (Rallison & Hinch 1986) in appropriate limits. Leshansky & Brady (2005) carefully described the theory and applied it to shear-induced diffusion. Here, we briefly sketch the argument. Note that the analysis would lose its validity in the case of drop coalescence or break-up which are not considered here. In dynamic light scattering, the scattered light corresponding to the scattered wavenumber k (non-dimensionalized by a) from N scatterers located at $x'_\alpha(t')$, $\alpha = 1, 2, \ldots, N$ is proportional to the intermediate scattering function

$$F(\boldsymbol{k}, t') = \frac{1}{N} \left\langle \sum_{\alpha, \beta=1}^{N} e^{i\boldsymbol{k} \cdot (\boldsymbol{x}'_\alpha(t') - \boldsymbol{x}'_\beta(0))} \right\rangle. \tag{4.3}$$

Note that by the property of the Dirac delta function, the number density of the scatterers (here droplets) and its spatial Fourier transform can be written as

$$n(\boldsymbol{x}', t') = \sum_{\alpha=1}^{N} \delta(\boldsymbol{x}' - \boldsymbol{x}'_\alpha), \quad \hat{n}(\boldsymbol{k}, t') = \sum_{\alpha=1}^{N} e^{i\boldsymbol{k} \cdot \boldsymbol{x}'_\alpha}. \tag{4.4a,b}$$

Therefore, $F(\boldsymbol{k}, t') = 1/N \langle \hat{n}(\boldsymbol{k}, t') \hat{n}^*(\boldsymbol{k}, 0) \rangle$ may be regarded as measuring the autocorrelation of the fluctuation $n'(\boldsymbol{x}', t')$ (where $n(\boldsymbol{x}', t) = n_o + n'(\boldsymbol{x}', t')$) at wavenumber $\boldsymbol{k}$ for a statistically homogeneous system, as the constant background n_o would not contribute to the autocorrelation. Our system is not homogeneous, but evolves from a non-homogeneous initial condition with a strong concentration gradient. However, one can note the following. Leshansky & Brady (2005) showed that the theory assumes a model of the number density satisfying an advection diffusion equation in a shear flow $\boldsymbol{U} + \dot{\boldsymbol{\Gamma}} \cdot \boldsymbol{x}$ ($\boldsymbol{U}$ is the average flow and $\dot{\boldsymbol{\Gamma}}$ is the velocity gradient tensor):

$$\frac{\partial n}{\partial t'} + (\boldsymbol{U} + \dot{\boldsymbol{\Gamma}} \cdot \boldsymbol{x}) \cdot \nabla n = \boldsymbol{D}_c \nabla^2 n. \tag{4.5}$$

One can use the same governing equation here, but unlike the homogeneous case considered by the previous authors, the initial condition for (4.5) here is different and represents the droplets concentrated in the central layer. Therefore, whereas the concentration variation in the previous case results from the fluctuations caused by the interactions of moving drops, here we introduce an initial inhomogeneous concentration variation. But (4.5) is linear and therefore, the different wavenumber components $\hat{n}(\boldsymbol{k}, t')$ are independent and the theory remains valid. One possible concern is the value of the diffusivity obtained being dependent on the strength of the variation and, in principle, one has to calculate for different strengths and the results extrapolated to zero as was also argued by Marchioro & Acrivos (2001) for one of their proposed methods for the computation of collective diffusivity. (Note that (4.5) is slightly different from the one in Leshansky & Brady (2005), where a non-local Fick's law of diffusion was used to mathematically derive the expression governing the wavenumber dependent diffusivity in the Fourier domain. Alternatively one can postulate an independent linear Fick's law in the Fourier domain (Russel & Glendinning 1981).)

In spite of the advection terms in (4.5), in a simple shear due to the orthogonality of the $\boldsymbol{k}(= k\hat{\boldsymbol{y}})$ vector to the velocity field, one obtains a simple relation for the diffusivity in the gradient direction (Leshansky & Brady 2005):

$$D_{c,yy} = -\frac{1}{k^2}\frac{\mathrm{d}(\ln F)}{\mathrm{d}t'}. \tag{4.6}$$

Note that instead of F, if one uses the self-intermediate scattering function F_s defined by

$$F_s(\boldsymbol{k}, t') = \frac{1}{N}\left\langle \sum_{\alpha=1}^{N} \mathrm{e}^{\mathrm{i}\boldsymbol{k}\cdot(\boldsymbol{x}'_\alpha(t) - \boldsymbol{x}'_\alpha(0))} \right\rangle, \tag{4.7}$$

one obtains long-term self-diffusivity $D_{s,yy}^\infty$ from the same equation (4.6) (Morris & Brady 1996). We compute $F(\boldsymbol{k}, t')$ according to (4.3) using the simulated drop evolution data positions after eliminating the initial part ($t'_0 = 20$). The resulting intermediate scattering functions are averaged over overlapping intervals to obtain a smooth time evolution curve as was also executed by Leshansky & Brady (2005). In figure 11(*a*), we plot $-\ln F(\boldsymbol{k}', t)/k^2$ for $Ca = 0.05$ for different wavenumbers normalizing their initial values. They show a linear growth with time and the curves tend to converge to a single curve in the small k limit. Accordingly, the slope of the curves asymptotes to a value as $k \to 0$ (large length scale limit), as shown in figure 11(*c*) for different Ca values. Figure 11(*d*) plots this asymptotic value of the slope, i.e. the collective diffusivity $D_{c,yy}$ (non-dimensionalized by a and $\dot{\gamma}$) as a function of Ca. Similar to f_2 in figure 8, $D_{c,yy}$ shows a non-monotonic behaviour with Ca. Due to the spatial variation and continuous decrease in the local volume fraction $\varphi(y', t')$ with time, one cannot directly compare the two values. However, the approximate ratio $D_{c,yy}/f_2 \sim 0.1$ can be recognized as an average $\varphi \sim 0.1$ starting with a maximum local value of 0.25 (see figure 3*b*).

As noted before, unlike in Leshansky & Brady (2005), the results here are obtained from the evolution of an initially prescribed inhomogeneity instead of spontaneously occurring fluctuations. The scaled parabolic evolution (3.2) of the imposed initial condition also explains the increasing trend of the slope of $-\ln F(\boldsymbol{k}, t')/k^2$ with k in figure 11(*c*). To further elucidate this fact, we interrogate the parabolic concentration profile $\bar{n}(y', t') = 3\varphi(y', t')/4\pi a^3$ fitted at successive time instants from the simulated droplet positions (as in figure 3*b*). We compute fast Fourier transform (FFT) of the data $\hat{\bar{n}}(k, t')$ and find the corresponding autocorrelation $\bar{F}(k, t') = 1/N\langle\hat{\bar{n}}(k, t')\hat{\bar{n}}^*(k, 0)\rangle$. The time evolution was averaged following a procedure identical to the one for $F(\boldsymbol{k}, t')$. For $Ca = 0.05$ in figure 11(*b*), $-\ln \bar{F}(k, t')/k^2$ shows behaviour very similar to that of $-\ln F(\boldsymbol{k}, t')/k^2$ shown in figure 11(*a*) derived directly from the discrete particle positions. The slopes at different k and Ca from the fitted parabolic profiles plotted in figure 11(*c*) also follow the same curve. In figure 11(*d*), the dashed line from this procedure matches the one computed from discrete positions directly. Therefore, we emphasize that the increasing trend of the slope of $-\ln F(\boldsymbol{k}, t')/k^2$ in figure 11(*c*) arises from the nonlinear diffusion of the imposed initial condition. For the same reason, interpretation of the values of $-\ln F(\boldsymbol{k}, t')/k^2$ for higher k as wavenumber dependent diffusivity is not possible here. Note that in the limit of $k \to \infty$, in (4.3) due to the large variations in the phase factors for terms corresponding to $\alpha \neq \beta$ results in $F(\boldsymbol{k}, t') \to F_s(\boldsymbol{k}, t')$ (Rallison & Hinch 1986; Leshansky & Brady 2005). Therefore, the slope of $-\ln F(\boldsymbol{k}, t')/k^2$ in this limit gives rise to self-diffusivity. However, with the small system size (which becomes more acute for the single summation in (4.7)),
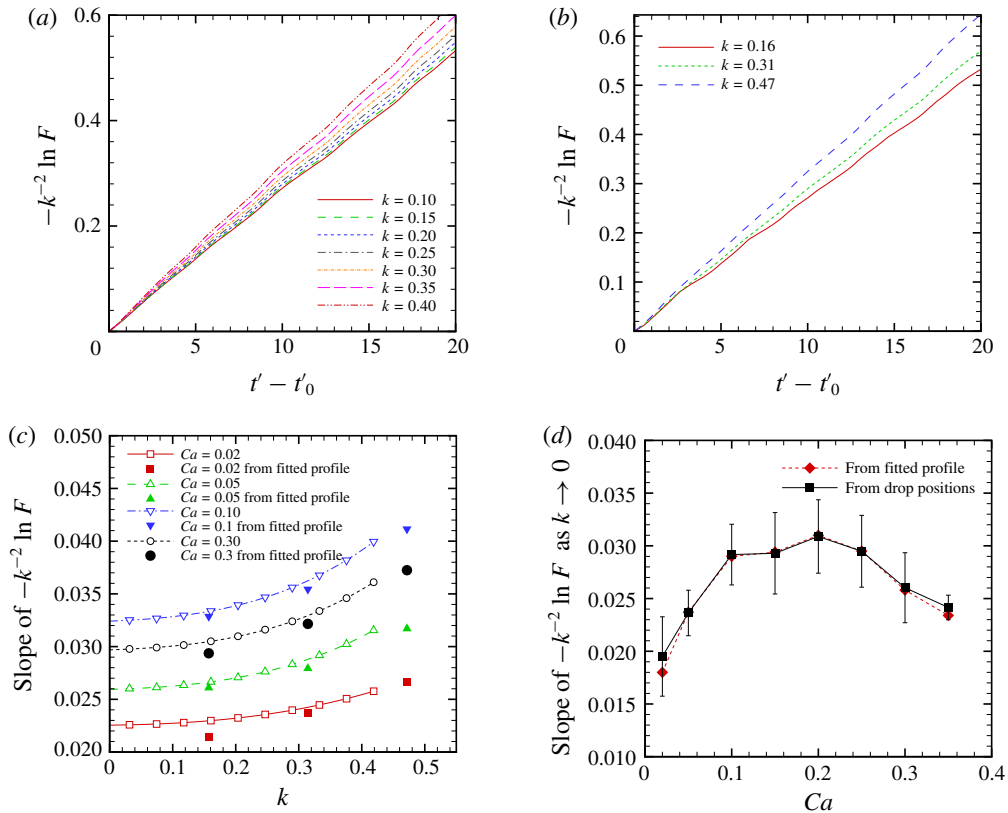
FIGURE 11. (Colour online) (*a*) The dependence of $-\ln F(\boldsymbol{k}, t')/k^2$ on time for various wavenumbers obtained from individual particle positions. (*b*) The same computed using the autocorrelation function of the fitted parabolic concentration profile. (*c*) Slope of $-\ln F(\boldsymbol{k}, t')/k^2$ as a function of the wavenumber for both the previous calculations showing similar values. (*d*) Slope of $-\ln F(\boldsymbol{k}, t')/k^2$ at the lowest wavenumber obtained from both calculations. The dependence on Ca is similar to what was obtained for f_2 versus Ca (figure 8).

the values of self-diffusivity computed using (4.7) were too noisy to be quantitatively useful, although they were of the right magnitude (smaller by a factor of 5 compared to the gradient diffusivity). In any event, the above analysis demonstrates that the procedure for computation of dynamic structure factor and correspondingly the collective diffusivity can also be applied to inhomogeneous systems. We also note the following about our method *vis-à-vis* the dynamic structure factor method. In a statistically homogeneous or non-homogeneous (as in here) system, the accuracy of the results obtained from a particular analysis, to which one subjects the experimental or the simulated data (e.g. the droplet positions here) depends on the validity of the assumptions of the theory underlying the analysis. The dynamic structure factor theory assumes a linear governing equation (4.5), whereas the results obtained before based on the observed $\sim t^{1/3}$ scaling indicates a nonlinear diffusion (3.2) with $D_{c,yy}$ linear in φ or n. One can apply dynamic structure factor theory to simulations performed at different volume fractions, and obtain volume fraction dependence of diffusivity, as was executed by Leshansky & Brady (2005). However, the implicit assumption is

that during the time of analysis the variation in the fluctuation remains sufficiently small so that the linear theory remains. Nonetheless, we argue that different analytical procedures can provide fruitful information about a system as long as their underlying assumptions are kept in mind.

5. Summary and concluding remarks

In summary, we have used fully resolved numerical simulations to compute the gradient or collective diffusivity of viscous drops in a sheared emulsion. We used two slightly different methods – the width of a fitted concentration profile, and the standard deviation of the droplet positions – using a relatively small number (70) of droplets. Both yielded very similar results and were roughly consistent with the single experimental observation available in the literature, as well as the limit value of a previous theoretical computation. The collective diffusivity was seen to vary non-monotonically with Ca, due to the competition between the increasing deformation and decreasing inclination in the underlying drop dynamics, which in turn affects the drop–drop collision. An empirical correlation has been developed to describe the Ca dependence. We also applied an alternative method of computing collective diffusivity, using the dynamic structure factor, that was originally developed for statistically homogeneous suspensions. Although the results could not be directly compared, as the system is inhomogeneous, we show that the results from the alternative method when appropriately interpreted are in qualitative agreement with those from the other method including the prediction of the non-monotonic variation with capillary number. It indicates that the structure factor based method could provide valuable information even in a non-homogeneous system. In future, effects of viscosity ratio variation as well as more complex systems such as suspensions of capsules or vesicles will be investigated.

Acknowledgements

Supplementary movie

Supplementary movie is available at https://doi.org/10.1017/jfm.2019.122.

REFERENCES

ALTENBERGER, A. R. 1979 On the wave vector dependent mutual diffusion of interacting Brownian particles. *J. Chem. Phys.* **70** (4), 1994–2002.

ALTENBERGER, A. R. & DEUTCH, J. M. 1973 Light scattering from dilute macromolecular solutions. *J. Chem. Phys.* **59** (2), 894–898.

BATCHELOR, G. K. 1972 Sedimentation in a dilute dispersion of spheres. *J. Fluid Mech.* **52** (2), 245–268.

BATCHELOR, G. K. & GREEN, J. T. 1972 Determination of bulk stress in a suspension of spherical-particles to order C-2. *J. Fluid Mech.* **56** (Dec 12), 401–427.

BERNE, B. J. & PECORA, R. 1976 *Dynamic Light Scattering: With Applications to Chemistry, Biology, and Physics*. Wiley.

BRADY, J. F. & BOSSIS, G. 1988 Stokesian dynamics. *Annu. Rev. Fluid Mech.* **20** (1), 111–157.

BREEDVELD, L. V. A. 2000 Shear-induced self-diffusion in concentrated suspensions. PhD thesis.

BREEDVELD, V., VAN DEN ENDE, D., TRIPATHI, A. & ACRIVOS, A. 1998 The measurement of the shear-induced particle and fluid tracer diffusivities in concentrated suspensions by a novel method. *J. Fluid Mech.* **375**, 297–318.

BUREAU, L., COUPIER, G., DUBOIS, F., DUPERRAY, A., FARUTIN, A., MINETTI, C., MISBAH, C., PODGORSKI, T., TSVIRKUN, D. & VYSOKIKH, M. 2017 Blood flow and microgravity. *C. R. Méc.* **345** (1), 78–85.

CHA, W. & BEISSINGER, R. L. 2001 Evaluation of shear-induced particle diffusivity in red cell ghosts suspensions. *Korean J. Chem. Engng* **18** (4), 479–485.

CHAFFEY, C. E. & BRENNER, H. 1967 A second order theory for shear deformation of drops. *J. Colloid Interface Sci.* **24** (2), 258–269.

CHAN, P. C. H. & LEAL, L. G. 1979 The motion of a deformable drop in a second-order fluid. *J. Fluid Mech.* **92** (01), 131–170.

COOKE, B. M., MOHANDAS, N. & COPPEL, R. L. 2001 The malaria-infected red blood cell: structural and functional changes. *Adv. Parasitol.* **50**, 1–86.

DA CUNHA, F. & HINCH, E. J. 1996 Shear-induced dispersion in a dilute suspension of rough spheres. *J. Fluid Mech.* **309**, 211–223.

DAVIS, R. H. 1996 Hydrodynamic diffusion of suspended particles: a symposium. *J. Fluid Mech.* **310**, 325–335.

DESMOND, K. & WEEKS, E. 2009 Random close packing of disks and spheres in confined geometries. *Phys. Rev.* E **80** (5), 051305.

ECKSTEIN, E. C., BAILEY, D. G. & SHAPIRO, A. H. 1977 Self-diffusion of particles in shear flow of a suspension. *J. Fluid Mech.* **79** (01), 191–208.

FOSS, D. R. & BRADY, J. F. 1999 Self-diffusion in sheared suspensions by dynamic simulation. *J. Fluid Mech.* **401**, 243–274.

GIRES, P.-Y., SRIVASTAV, A., MISBAH, C., PODGORSKI, T. & COUPIER, G. 2014 Pairwise hydrodynamic interactions and diffusion in a vesicle suspension. *Phys. Fluids* **26** (1), 013304.

GOLDSMITH, H. L. & MARLOW, J. C. 1979 Flow behavior of erythrocytes. II. Particle motions in concentrated suspensions of ghost cells. *J. Colloid Interface Sci.* **71** (2), 383–407.

GRANDCHAMP, X., COUPIER, G., SRIVASTAV, A., MINETTI, C. & PODGORSKI, T. 2013 Lift and down-gradient shear-induced diffusion in red blood cell suspensions. *Phys. Rev. Lett.* **110** (10), 108101.

HIGGINS, J. M., EDDINGTON, D. T., BHATIA, S. N. & MAHADEVAN, L. 2009 Statistical dynamics of flowing red blood cells by morphological image processing. *PLOS Comput. Biol.* **5** (2), e1000288.

HUDSON, S. D. 2003 Wall migration and shear-induced diffusion of fluid droplets in emulsions. *Phys. Fluids* **15** (5), 1106–1113.

KING, M. R. & LEIGHTON, D. T. 2001 Measurement of shear-induced dispersion in a dilute emulsion. *Phys. Fluids* **13** (2), 397–406.

LEIGHTON, D. T. & ACRIVOS, A. 1987 Measurement of shear-induced self-diffusion in concentrated suspensions of spheres. *J. Fluid Mech.* **177**, 109–131.

LESHANSKY, A. M. & BRADY, J. F. 2005 Dynamic structure factor study of diffusion in strongly sheared suspensions. *J. Fluid Mech.* **527**, 141–169.

LESHANSKY, A. M., MORRIS, J. F. & BRADY, J. F. 2008 Collective diffusion in sheared colloidal suspensions. *J. Fluid Mech.* **597**, 305–341.

LI, X. & SARKAR, K. 2008 Front tracking simulation of deformation and buckling instability of a liquid capsule enclosed by an elastic membrane. *J. Comput. Phys.* **227** (10), 4998–5018.

LOEWENBERG, M. & HINCH, E. J. 1997 Collision of two deformable drops in shear flow. *J. Fluid Mech.* **338**, 299–315.

LOPEZ, M. & GRAHAM, M. D. 2008 Enhancement of mixing and adsorption in microfluidic devices by shear-induced diffusion and topography-induced secondary flow. *Phys. Fluids* **20** (5), 053304.

MARCHIORO, M. & ACRIVOS, A. 2001 Shear-induced particle diffusivities from numerical simulations. *J. Fluid Mech.* **443**, 101–128.

MORRIS, J. F. & BRADY, J. F. 1996 Self-diffusion in sheared suspensions. *J. Fluid Mech.* **312**, 223–252.

MUKHERJEE, S. & SARKAR, K. 2009 Effects of viscosity ratio on deformation of a viscoelastic drop in a Newtonian matrix under steady shear. *J. Non-Newtonian Fluid Mech.* **160** (2–3), 104–112.

MUKHERJEE, S. & SARKAR, K. 2013 Effects of matrix viscoelasticity on the lateral migration of a deformable drop in a wall-bounded shear. *J. Fluid Mech.* **727**, 318–345.

MUKHERJEE, S. & SARKAR, K. 2014 Lateral migration of a viscoelastic drop in a Newtonian fluid in a shear flow near a wall. *Phys. Fluids* **26** (10), 103102.

OLAPADE, P. O., SINGH, R. K. & SARKAR, K. 2009 Pairwise interactions between deformable drops in free shear at finite inertia. *Phys. Fluids* **21** (6), 063302.

PODGORSKI, T., CALLENS, N., MINETTI, C., COUPIER, G., DUBOIS, F. & MISBAH, C. 2011 Dynamics of vesicle suspensions in shear flow between walls. *Microgravity Sci. Technol.* **23** (2), 263–270.

RALLISON, J. M. & HINCH, E. J. 1986 The effect of particle interactions on dynamic light scattering from a dilute suspension. *J. Fluid Mech.* **167**, 131–168.

RAMACHANDRAN, A., LOEWENBERG, M. & LEIGHTON, D. T. 2010 A constitutive equation for droplet distribution in unidirectional flows of dilute emulsions for low capillary numbers. *Phys. Fluids* **22** (8), 083301.

RUSCONI, R. & STONE, H. A. 2008 Shear-induced diffusion of platelike particles in microchannels. *Phys. Rev. Lett.* **101**, 254502.

RUSSEL, W. B. & GLENDINNING, A. B. 1981 The effective diffusion coefficient detected by dynamic light scattering. *J. Chem. Phys.* **74** (2), 948–952.

SARKAR, K. & SCHOWALTER, W. R. 2000 Deformation of a two-dimensional viscoelastic drop at non-zero Reynolds number in time-periodic extensional flows. *J. Non-Newtonian Fluid Mech.* **95** (2–3), 315–342.

SARKAR, K. & SCHOWALTER, W. R. 2001 Deformation of a two-dimensional drop at non-zero Reynolds number in time-periodic extensional flows: numerical simulation. *J. Fluid Mech.* **436**, 177–206.

SARKAR, K. & SINGH, R. K. 2013 Spatial ordering due to hydrodynamic interactions between a pair of colliding drops in a confined shear. *Phys. Fluids* **25** (5), 051702.

SIEROU, A. & BRADY, J. F. 2004 Shear-induced self-diffusion in non-colloidal suspensions. *J. Fluid Mech.* **506**, 285–314.

SINGH, R. K., LI, X. & SARKAR, K. 2013 Lateral migration of a capsule in plane shear near a wall. *J. Fluid Mech.* **739**, 421–443.

SINGH, R. K. & SARKAR, K. 2009 Effects of viscosity ratio and three dimensional positioning on hydrodynamic interactions between two viscous drops in a shear flow at finite inertia. *Phys. Fluids* **21** (10), 103303.

SINGH, R. K. & SARKAR, K. 2015 Hydrodynamic interactions between pairs of capsules and drops in a simple shear: Effects of viscosity ratio and heterogeneous collision. *Phys. Rev.* E **92** (6), 063029.

SRIVASTAVA, P., MALIPEDDI, A. R. & SARKAR, K. 2016 Steady shear rheology of a viscous emulsion in the presence of finite inertia at moderate volume fractions: sign reversal of normal stress differences. *J. Fluid Mech.* **805**, 494–522.

TAN, M. H.-Y., LE, D.-V. & CHIAM, K.-H. 2012 Hydrodynamic diffusion of a suspension of elastic capsules in bounded simple shear flow. *Soft Matt.* **8**, 2243–2251.

TAYLOR, G. I. 1934 The formation of emulsions in definable fields of flow. *Proc. R. Soc. Lond.* A **146** (A858), 0501–0523.

TOWNS, J., COCKERILL, T., DAHAN, M., FOSTER, I., GAITHER, K., GRIMSHAW, A., HAZLEWOOD, V., LATHROP, S., LIFKA, D., PETERSON, G. D., ROSKIES, R., SCOTT, J. R. & WILKINS-DIEHR, N. 2014 XSEDE: accelerating scientific discovery. *Comput. Sci. Engng* **16** (5), 62–74.

TRYGGVASON, G., BUNNER, B., ESMAEELI, A., JURIC, D., AL-RAWAHI, N., TAUBER, W., HAN, J., NAS, S. & JAN, Y.-J. 2001 A front-tracking method for the computations of multiphase flow. *J. Comput. Phys.* **169** (2), 708–759.

WANG, Y., MAURI, R. & ACRIVOS, A. 1998 Transverse shear-induced gradient diffusion in a dilute suspension of spheres. *J. Fluid Mech.* **357**, 279.

ZHAO, H. & SHAQFEH, E. S. G. 2013 The dynamics of a non-dilute vesicle suspension in a simple shear flow. *J. Fluid Mech.* **725**, 709–731.

ZINCHENKO, A. Z. & DAVIS, R. H. 2002 Shear flow of highly concentrated emulsions of deformable drops by numerical simulations. *J. Fluid Mech.* **455**, 21–62.